nature nanotechnology

Article

https://doi.org/10.1038/s41565-023-01316-3

Imaging solid–electrolyte interphase dynamics using operando reflection interference microscopy

Received: 23 February 2022

Accepted: 3 January 2023

Published online: 09 February 2023

Check for updates

Guangxia Feng[1,7], Hao Jia[2,7], Yaping Shi[1,7], Xu Yang[1], Yanliang Liang[1], Mark H. Engelhard[3], Ye Zhang[4], Chaojie Yang[1], Kang Xu[5] ✉, Yan Yao[1,4,6] ✉, Wu Xu[2] ✉ & Xiaonan Shan[1] ✉

The quality of the solid–electrolyte interphase is crucial for the performance of most battery chemistries, but its formation dynamics during operation are not well understood due to a lack of reliable operando characterization techniques. Herein, we report a dynamic, non-invasive, operando reflection interference microscope to enable the real-time imaging of the solid–electrolyte interphase during its formation and evolution processes with high sensitivity. The stratified structure of the solid–electrolyte interphase formed during four distinct steps includes the emergence of a permanent inner inorganic layer enriched in LiF, a transient assembly of an interfacial electrified double layer and a consequent emergence of a temporary outer organic-rich layer whose presence is reversible with electrochemical cycling. Reflection interference microscope imaging reveals an inverse correlation between the thicknesses of two interphasial subcomponents, implying that the permanent inorganic-rich inner layer dictates the organic-rich outer layer formation and lithium nucleation. The real-time visualization of solid–electrolyte interphase dynamics provides a powerful tool for the rational design of battery interphases.

Lithium (Li)-ion batteries (LIBs) have transformed modern electronic devices and are used for electric vehicles and in the grid energy storage industry[1–5]. However, the demand for higher energy density has persistently pressed researchers to develop new battery chemistries[2,6–12]. The Li metal anode holds promise as the ultimate anode material due to the combination of its ultrahigh theoretical specific capacity and lowest electrochemical redox potential, while an 'anode-free' configuration that generates an in situ Li anode makes the goal of 500 Wh kg^{-1} possible[13–16]. The interphase in 'anode-free' cells differs from those formed in either conventional LIBs or Li metal batteries (LMBs), with mixed characteristics of both the stepwise (or discriminating) nature of the former and the instantaneous (or indiscriminating) nature of the latter[17]. Hence, this interphase presents the most interesting and meaningful case for a fundamental understanding of interphases. In such cells, during the initial charging process, the potential of the bare copper (Cu) foil is brought progressively below the lowest unoccupied molecular orbital (LUMO) energy of the electrolyte, thus triggering an irreversible reaction and forming the primitive solid–electrolyte

[1]Department of Electrical and Computer Engineering, University of Houston, Houston, TX, USA. [2]Energy and Environment Directorate, Pacific Northwest National Laboratory, Richland, WA, USA. [3]Environmental Molecular Sciences Laboratory, Pacific Northwest National Laboratory, Richland, WA, USA. [4]Materials Science and Engineering Program, University of Houston, Houston, TX, USA. [5]Battery Science Branch, Energy Science Division, Sensor and Electron Devices Directorate, Army Research Laboratory, Adelphi, MD, USA. [6]Texas Center for Superconductivity at the University of Houston, University of Houston, Houston, TX, USA. [7]These authors contributed equally: Guangxia Feng, Hao Jia, Yaping Shi. ✉e-mail: conrad.k.xu.civ@army.mil; yyao4@uh.edu; wu.xu@pnnl.gov; xshan@central.uh.edu

interphase (SEI). This proto-SEI experiences further evolutions as the Cu foil is polarized more cathodically, while the emergence of Li at lower potential induces instantaneous reactions with the bulk electrolyte, forming the second round of interphasial chemicals. Such an interphase on Cu and Li surfaces stabilizes the electrolyte against reductive decomposition by blocking electron tunnelling while still allowing Li^+ to migrate, so that the battery operates reversibly without sustained electrolyte decomposition[18–20]. Therefore, the SEI holds the key to the next generation high-energy batteries.

To understand the physical and chemical aspects of the SEI formed in LIBs and LMBs, various advanced analytical techniques have been developed and explored. Ex situ studies including scanning electron microscopy[21], transmission electron microscopy[22,23], Fourier-transform infrared spectroscopy[24–26], Raman spectroscopy[27–29] and X-ray photoelectron spectroscopy (XPS)[30–32] reveal important local information regarding the structural and chemical natures of SEIs. High-energy electron and X-ray beams, on the other hand, inevitably cause damage to the fragile SEI, resulting in artefacts. In situ secondary ion mass spectrometry[33] identifies the precise SEI chemical composition, but structural and morphological information is lacking. Ex situ cryogenic electron microscopy, inspired by biological imaging methods, is an extremely powerful tool that has been successfully employed to retain the native state of the SEI during high-resolution electron imaging at cryogenic conditions[34,35]. This technique enables atomic-resolution imaging of SEI layers and Li dendrites, although it only shows static and cross-sectional information, leaving out the dynamic evolution of the SEI during charge–discharge cycles. In situ atomic force microscopy (AFM) offers the vivid morphological changes of the SEI[36–38]; nevertheless, its relatively modest scan speed restricts its capability to map the dynamic processes, and chemical information is lacking. Finally, while an electrochemical quartz crystal microbalance device accurately measures the mass change induced by the SEI formation[39], it lacks local information on the distribution of chemical components, which may be critical for evaluating the SEI quality. Most importantly, the 'hybrid' complexity of 'anode-free' SEIs and how the two sublayers correlate with Li^0 nucleation kinetics have never been recognized, let alone investigated or understood, to the best of our knowledge.

In this work, we seek to bridge the gap in the current techniques. We directly image and map the formation dynamics of an SEI on a Cu surface and the subsequent transformation at the emergence of Li, as well as the evolution of the SEI over many cycles, using an operando reflection interference microscopy (RIM) with high sensitivity as well as high temporal and spatial resolution, on a half-cell that simulates the in situ formation of Li in an 'anode-free' LMB. The interference created by the top and bottom surfaces of various SEI strata provides high sensitivity to detect minimal signals generated from any interfacial events. To create a high-resolution focused image, a multi-immersion objective is used in an open-cell set-up. The electrolyte consisting of 1 M $LiPF_6$ in propylene carbonate (PC) was chosen as the benchmark because it has been extensively researched using various techniques, and its chemical pathways are well established[40,41]. We successfully monitored the entire evolution process of the SEI layer in real time using RIM. The formation and stripping of the SEI are discovered to be a multi-step process that includes the formation of a proto-SEI based on a LiF-containing inorganic layer, the assembly of an electrical double layer (EDL) interface and the reversible emergence and disappearance of a transient organic-rich SEI layer. The formation of this LiF-rich inner layer dominates the process in the first cycle, and it gradually evolves into a permanent interphase layer throughout subsequent cycles. The organic-rich outer layer, on the other hand, emerges after the formation of LiF-rich proto-SEI and fades in each cycle, depending on the electrode potential. We also observed the continuous charge accumulation and depletion at the EDL even after the formation of the permanent LiF-rich SEI layer, which does not block Li^+ transport.

RIM provides information over the entire reaction process at the same location and allows us to study the interactions of different interphasial processes, including the LiF-rich and organic-rich SEI layers' formation, charge accumulation and Li nucleation. We were able to translate the optical signals into localized morphology maps of a LiF-rich inner layer and an organic-rich outer layer, separately, and thus quantitatively revealed the strong inverse correlation between the thicknesses of the LiF-rich inner layer and the organic-rich outer layer; that is, the thicker the LiF-rich inner layer is, the thinner the organic-rich outer layer. This correlation is strengthened by the presence of trace amounts of water, which are intentionally introduced to promote HF formation, resulting in a considerably thicker and more-uniform LiF-rich inner layer, reduced electrolyte consumption and more-uniform Li nucleation on the electrode surface. The growth rates of the LiF-rich and organic-rich SEI layers are also extracted. Note that RIM requires accurate information of the refractive index to translate the optical signal to the corresponding absolute thickness. In this work, we have performed calibration experiments to measure the refractive index. In addition, we focus more on the dynamic and relative changes in the SEI formation and stripping processes and their evolutions over time, instead of an absolute thickness value. Knowledge of the dynamic evolution of the SEI during cell cycling and in the presence of electrolyte additives provides useful guidelines for the customized designing of interphases for high-performance batteries.

Imaging local surface reactions with RIM

In the initial charge, the potential of Cu is progressively polarized cathodically, and the electrolyte component (solvent, salt and additive) with the highest LUMO energy will be preferentially reduced, generating the primitive chemical ingredients for the proto-SEI. The proto-SEI experiences further electrochemical reduction as Cu continues the cathodic polarization, until Li^0 is deposited and the eventual permanent interphase is formed. An operando imaging method (that is, RIM) is hence applied to map the local emergence and distribution of SEI components generated in the above process, and more importantly, to probe the dynamics of the deposition and stripping of the extremely reactive Li^0. Figure 1a schematically displays the working principle of RIM. The reflected light at the electrode–electrolyte junction, which will become the electrode–SEI and SEI–electrolyte junctions, respectively, after the SEI is formed (Fig. 1a, right), will interfere with each other, which, after proper translation, carries information about the phase delay created by the changes in the SEI layer. If a layer deposited on the electrode surface has a refractive index smaller than the surrounding electrolyte, the reflected optical intensity will increase; otherwise, it will decrease (see more discussions on calibration experiments for RIM in 'Converting reflectance to thickness' section in Methods, and in Supplementary Section 2).

To image the SEI formation on the electrode surface, a three-electrode system in an open cell is used (Fig. 1a), where the Cu foil serves as the working electrode, and two Li foils serve as the reference and counter electrodes, respectively. Such a half-cell simulates the anode side of the 'anode-free' LMB. The cell was first cycled within the voltage range of 2.3 V to 0.1 V versus Li/Li^+, in which the SEI was formed in a stepwise and discriminating manner, similar to what happens in the initial cycles of LIBs.

Formation of LiF-rich proto-SEI

First, we studied the SEI formation in 1 M $LiPF_6$ in PC with 50 ppm water as an additive. The optical reflectance of the Cu surface changes obviously in the first three cycles of cyclic voltametric (CV) scans (Fig. 1c), which is correlated with the applied potential and the electrochemical current response (red and black curves in Fig. 1d, respectively). At the beginning of the first cycle (~0–5 s), a reflectance decrease (marked by the black arrow in Fig. 1c) and a corresponding current spike (marked by the black arrow in Fig. 1d) are observed, which is attributed to the reduction of Cu oxide (CuO) on the Cu electrode surface that is a prevalent

https://doi.org/10.1038/s41565-023-01316-3

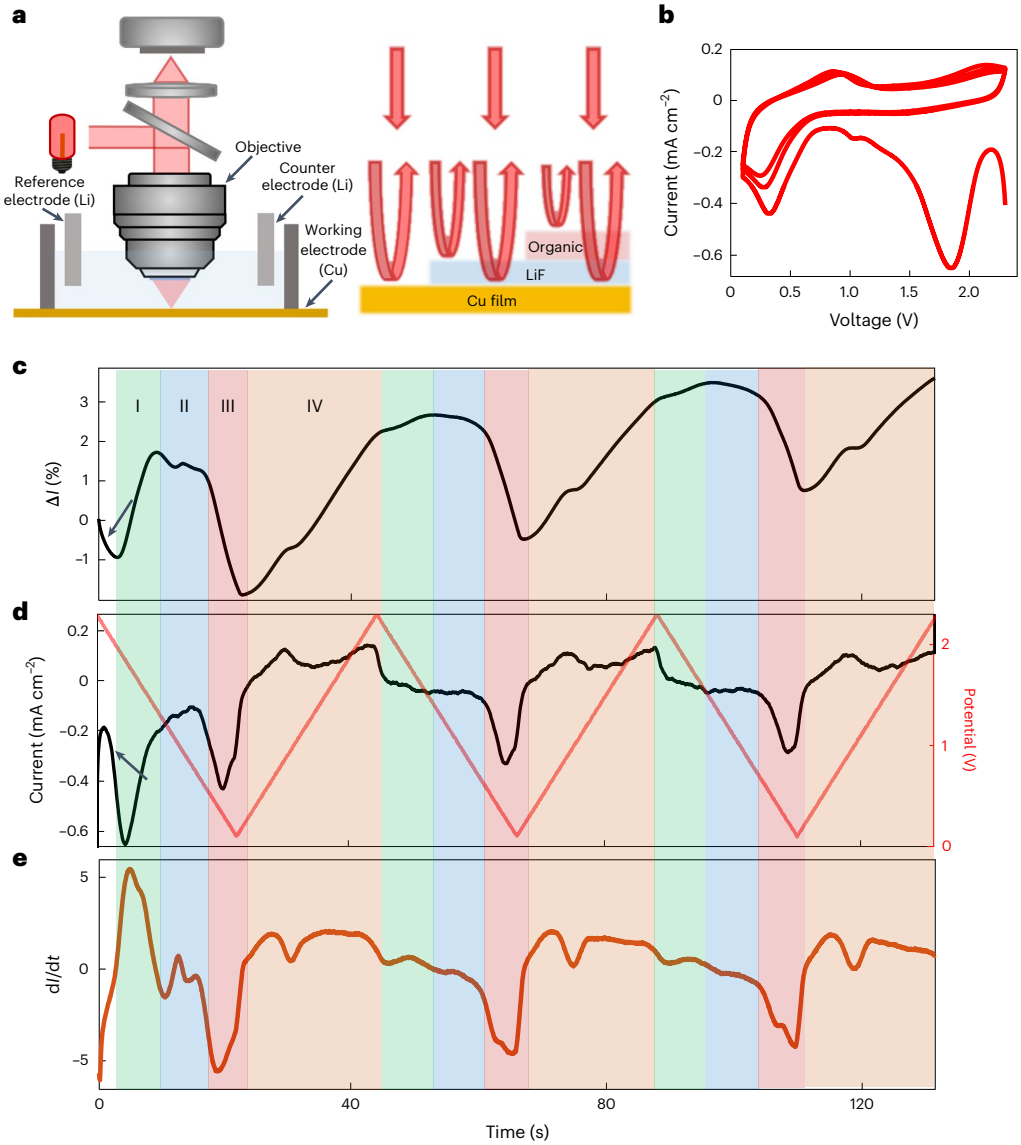

Fig. 1 | Operando characterization of SEI formation dynamics using RIM. **a**, Schematic diagram of using RIM to image the SEI formation dynamics. **b**, CV curves of the first three cycles in 1 M $LiPF_6$/PC with 50 ppm H_2O as additive. **c**, The optical reflection signal (RIM signal) during the first three CV cycles on the Cu electrode in 1 M $LiPF_6$/PC with 50 ppm H_2O additive. Sections I, II, III and IV correspond to LiF-rich layer formation (section I), EDL formation (section II), organic-rich SEI deposition (section III) and re-oxidization (section IV). **d**, The corresponding current density (black curve and left axis) and voltage (red curve and right axis) in the first three cycles of CV scans. The black arrows mark a feature that is described in the main text. **e**, The derivative of the optical signal (the curve in **c**). I, ΔI and t represent the intensity of optical signal, percentage change of optical signal and time, respectively.

result of ambient air exposure during the sample transfer[42]. After the CuO reduction, a current appears between 2.3 V and 1.3 V, which peaks around 1.8 V (Fig. 1d), accompanied by a substantial increase in the optical signal (the region highlighted with green shading in Fig. 1c). This process corresponds to the formation of a thin LiF-rich inorganic layer on the Cu surface that should definitely come from the salt anion PF_6^-, and the persistent presence of moisture in the electrolyte could be responsible via a diversified route (equations (1) and (2))[41,43].

$$LiPF_6 + H_2O \rightarrow 2HF + POF_3 + LiF \quad (1)$$

$$HF + Li^+ + e^- \rightarrow 0.5H_2 + LiF \quad (2)$$

The increase of optical responses in this section (section I in the figure) indicates the emergence of a layer that has a smaller refractive index than the electrolyte. Examining all the possible components of the SEI layer, we found that only LiF fits this description (Supplementary Section 2). To further validate the observation, a control experiment was conducted using the same electrolyte (1 M $LiPF_6$ in PC) without any water additive. We find that the optical responses in the same potential range are much smaller than those in the electrolyte in the presence of 50 ppm water (Supplementary Fig. 1a), indicating a much thinner deposition of the LiF-rich layer. Correspondingly, the HF reduction current (Supplementary Figs. 1b and 2) in the CV measurement is also decreased.

In the second section (section II with blue shading in Fig. 1c), a slightly decreased optical signal can be observed. Within this potential window of 1.3 V to 0.8 V (Fig. 1b) after the first cycle, the electrolyte mostly remains thermodynamically stable except that a minor electrochemical reaction happens at about 1 V in the first cathodic scan; therefore the change in optical signal should be attributed to the assembly

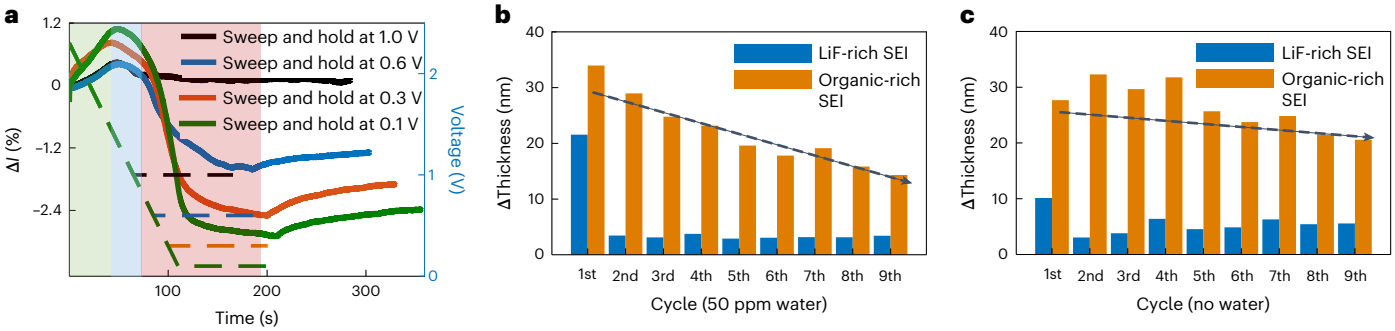

Fig. 2 | The growth and evolution of the SEI layers. a, Scan–hold–release experiments at different conditions. The solid lines are RIM signals in different experiments, and the dashed lines represent the corresponding potentials (reference to the right axis that is in blue colour to distinguish it from the left axis). The potential is scanned from 2.3 V to 1.0 V (black solid and dashed lines), to 0.6 V (blue solid and dashed lines), to 0.3 V (orange solid and dashed lines) and to 0.1V (green solid and dashed lines), and then held at the ending potentials for 100 s before released. The shading shows different stages, as described in the main text. **b**, The thickness increase (ΔThickness) of the LiF-rich layer (blue bars) and the organic-rich layer (orange bars) in each CV cycle in 1 M $LiPF_6$/PC with 50 ppm H_2O additive. **c**, The thickness increase (ΔThickness) of the LiF-rich layer (blue bars) and the organic-rich layer (orange bars) in each CV cycle in 1 M $LiPF_6$/PC without H_2O additive.

of Li^+ and the solvent molecules in its solvation sheaths to form an EDL on the deposited LiF layer. Note that the EDL should exist at the instant the electrode meets an electrolyte, but its structure evolves with both the applied voltage and the new morphology of the electrode surface. In this case, the deposition of LiF renders the electrode surface much rougher as compared with the pristine Cu surface. We used AFM to image the surface morphology before and after the LiF-rich SEI layer's deposition and found that the surface roughness increases from 0.6 nm to 1.1 nm (Supplementary Section 3). The surface roughness of the LiF-rich SEI layer (~1.1 nm in Supplementary Fig. 8) is very close to the value observed using RIM (~0.95 nm in Fig. 4h). This aggregation of solvated cations changes the structure and composition of the EDL only at the electrode–electrolyte interface, which is an interfacial behaviour of capacitive nature and has no impact on the permanent chemical composition of the SEI. On the other hand, the accumulation of charges on the electrode surface (in the metal film) will change the permittivity of the metal electrode surface and accordingly induce a decrease in the reflected optical intensity. The permittivity change in the solution caused by the EDL is negligible[44], and the signal correlated to the EDL comes from the opposite charge's accumulation in the metal film (more discussions on principle of RIM to image EDL are shown in Supplementary Section 4). Such EDL effects have been observed by RIM in our previous work[44,45]. Zhou et al. also reported an EDL established at the solid–liquid interface when the Cu electrode was charged to 1 V (ref. [33]). Furthermore, co-intercalation of solvated Li^+ was also observed when the graphite electrode was discharged to ~0.88 V (ref. [39]).

Reversible emergence and disappearance of organic-rich SEI

When the potential is lower than 0.8 V, the optical signal decreases substantially (section III with red shading in Fig. 1c). Correspondingly, the reduction current starts to increase quickly and peaks at 0.3 V. This corresponds to the reduction of carbonate solvents via a one-electron reduction process as described by equations (3) and (4) to generate Li_2CO_3 and Li alkyl carbonate[17]. The latter might be the priority pathway according to the literature[39,46].

$$C_4H_6O_3 + 2Li^+ + 2e^- \rightarrow Li_2CO_3 + C_3H_6 \quad (3)$$

$$2C_4H_6O_3 + 2Li^+ + 2e^- \rightarrow C_3H_6(OCO_2Li)_2 + C_3H_6 \quad (4)$$

As a result, the main composition of the reduced species is the organic component Li propylene dicarbonate (LPDC) from the $LiPF_6$/PC electrolyte, which constitutes an additional organic-rich SEI layer over the inorganic LiF-rich layer on the electrode surface[41]. Since the refractive index of the organic component is much higher than that of the electrolyte (Supplementary Section 2), the decrease in the optical signal also indicates that the deposited layer in this potential range (0.8 V to 0.1 V) is mainly enriched in organic species. When the scan direction is reversed from 0.1 V (that is, the anodic scan), the obtained optical signal continues to decrease, well in accordance with the current instead of the scan direction. This serves as a clear indication that the cathodic current in this region arises from the electrochemical decomposition of the electrolyte instead of the capacitive behaviour associated with the EDL.

In section IV (the section with orange shading in Fig. 1c), the electrochemical current starts to turn positive when the potential is higher than 0.25 V, with an anodic event at around 0.9 V. This indicates the reverse of the electrochemical reaction from reduction to oxidation on the electrode surface, and the accumulated organic-rich layer in the SEI is partially oxidized through equation (5)[47,48].

$$C_3H_6(OCO_2Li)_2 - 2e^- \rightarrow Li_2O + 2CO_2 + C_3H_6 + 0.5O_2 \quad (5)$$

The reversible emergence and disappearance of such nascent organic layers has been observed before on a graphitic surface with other techniques, such as AFM when an ethylene-carbonate-based (EC-based) electrolyte was used[49] or an electrochemical quartz crystal microbalance when a mixed carbonate electrolyte (EC/dimethyl carbonate (DMC)) was used[39]. It has been observed only during the initial cycles of the cell, and the oxidation seems to be partial only; that is, this organic layer cannot be completely removed. When the potential reaches a more positive region, the current and the differential of the optical response (Fig. 1c,e; discussion in Methods) both peak at around 0.9 V. The optical signal shows a obvious increase in Section IV (orange shading in Fig. 1c) during the oxidation process. This is due to the partial oxidation of the organic-rich layer, which leads to a decrease of the overall SEI presence on the electrode surface. There are also other non-electrochemical and parasitic reactions occurring simultaneously to consume the organic species in the SEI layer and cause the optical signal increase. For example, the HF generated from the hydrolysis of the salt anion (PF_6^-) will eliminate alkyl carbonate via equation (6)[50]. The Li_2CO_3 produced (from equation (3)) can also react with salt in the electrolyte via equation (7)[51].

$$C_3H_6(OCO_2Li)_2 + 2HF \rightarrow 2LiF + 2CO_2 + C_3H_6(OH)_2 \quad (6)$$

$$LiPF_6 + 2Li_2CO_3 \rightarrow 4LiF + 2CO_2 + F_2PO_2Li \quad (7)$$

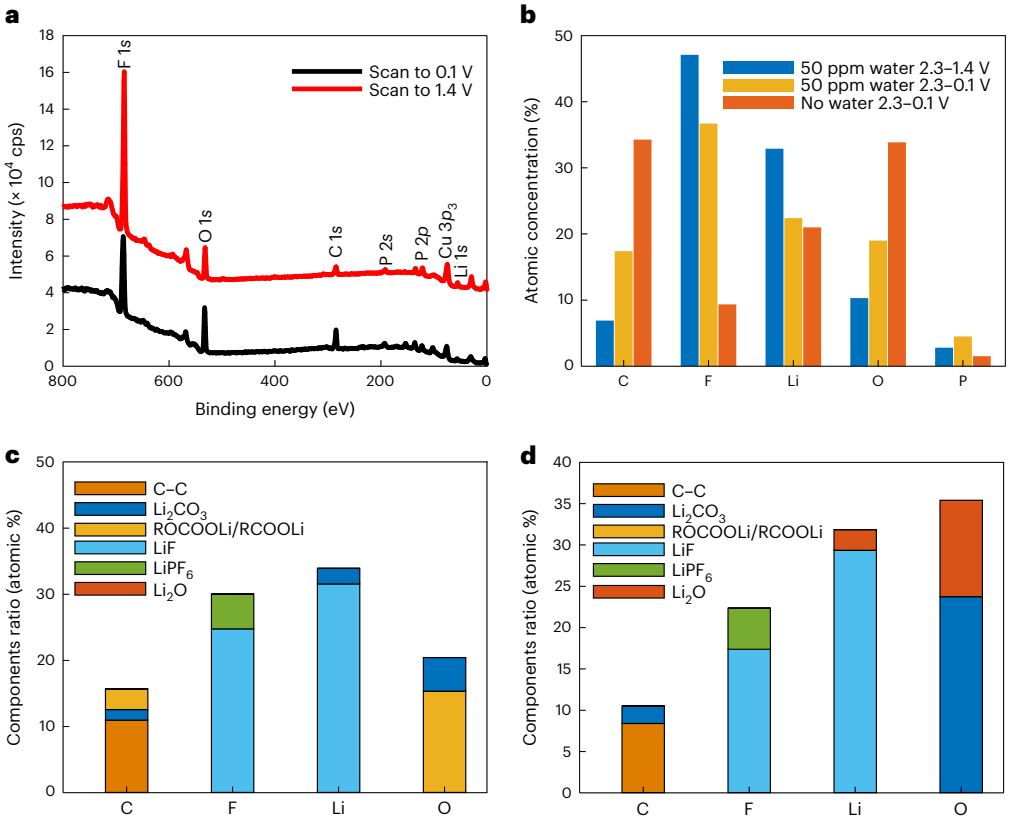

Fig. 3 | XPS analysis of the SEIs. a, XPS wide scan spectra of SEI formed at ending potentials of 1.4 V and 0.1 V in an electrolyte with 50 ppm water additive. **b**, Atomic concentrations of the SEI layers formed in different conditions. **c**,**d**, Relative concentrations of different chemicals measured at different depth of the SEI layer. Monoatomic Ar ion is used at low incident energies of 300 eV to remove the top layer of SEI. The ion beam raster area = 2 mm^2 and the calibrated sputter rate of 0.08 nm/s is based on a known thickness of Ta_2O_5/Ta. The sputtering times are 0 s (**c**) and 450 s (**d**).

These two possible chemical reaction pathways help account for the increase in the optical signal.

In the second and third cycles, the RIM response also shows four distinct sections that are similar to the first cycle (Fig. 1c, shaded with green, blue, red and orange). This means similar chemical processes and reactions are happening in the different cycles. In addition, the signal increase in section I of the later cycles (the growth of the LiF-rich layer) is relatively smaller than that of first cycle. We can also see a signal increase during the entire three cycles; this is due to the accumulation of LiF on the electrode surface over time (see more discussions in the 'Growth and evolution of SEI' section that follows).

Scan–hold–release experiments

To further verify observations obtained in the CV scans, a scan–hold–release experiment was performed. The potential was initially scanned from 2.3 V to different preselected cut-off potentials of 1.0 V, 0.6 V, 0.3 V and 0.1 V; subsequently held at these levels for 100 s; and finally released. The optical responses were recorded in Fig. 2a. At the early stage of the scan (from 2.3 V to 1.3 V), the increase of the optical reflection signals was apparent (highlighted with green shading in Fig. 2a). This correlates with the LiF formation on the electrode surface (section I in Fig. 1c). When the scan continued from 1.3 V to 0.8 V, the optical signal decreased, which corresponds to the EDL assembly (highlighted with blue shading in Fig. 2a and correlating with section II in Fig. 1c). When the potential is held at 1.0 V, over time, there is no obvious electrochemical reaction happening in this voltage range (from 1.3 V to 0.8 V), a flat line in the optical response was observed (black curve in Fig. 2a). When the potential was further decreased to 0.6 V, a decrease of optical reflectance occurred (blue curve in Fig. 2a), which indicates the formation of the organic-rich layer in SEI (highlighted with red shading in Fig. 2a and in section III of Fig. 1c). In addition, holding the potential at 0.6 V for 100 s led to a continuous decrease in the optical signal, indicating that the reduction continues and the organic-rich SEI layer keeps growing. For the 0.3 V (orange curve in Fig. 2a) and 0.1 V (green curve in Fig. 2a), the signal decreases in the red section are much bigger than that of 0.6 V. This is because a larger amount of organic-rich SEI was formed on the electrode. When the applied potentials (0.6 V, 0.3 V and 0.1 V) are removed, a fraction of the ions in the EDL are released from the interface, which causes the optical reflectance to increase initially. Furthermore, following signal stabilization, all three tests (0.6 V, 0.3 V and 0.1 V) exhibit substantially lower optical signals, indicating that the organic-rich outer layer stays on the electrode surface, and it will not diffuse away or dissolve automatically. These findings provide strong support for our observations of the dynamic formation of the SEI layers in the CV scans (see more discussions in Supplementary Section 5).

Growth and evolution of SEI

To understand the evolution and maturation of SEI over cycling, we performed the CV scans for nine cycles continuously and captured optical reflection data. The optical reflection signal variations were used to calculate the thicknesses of the SEI's LiF-rich inner and organic-rich outer layers for each cycle (details in Methods, Supplementary Section 6 and Supplementary Figs. 13 and 14). The bars in Fig. 2b,c show the thickness change (ΔThickness) in each cycle. The findings for 1 M $LiPF_6$/PC electrolytes in the presence and absence of 50 ppm water are described in Fig. 2b,c, respectively. Water appears to promote a thicker LiF-rich SEI layer (~23 nm, Fig. 2b) in the first cycle, as indicated by a substantially greater signal rise in section I in Fig. 1c (green colour),

https://doi.org/10.1038/s41565-023-01316-3

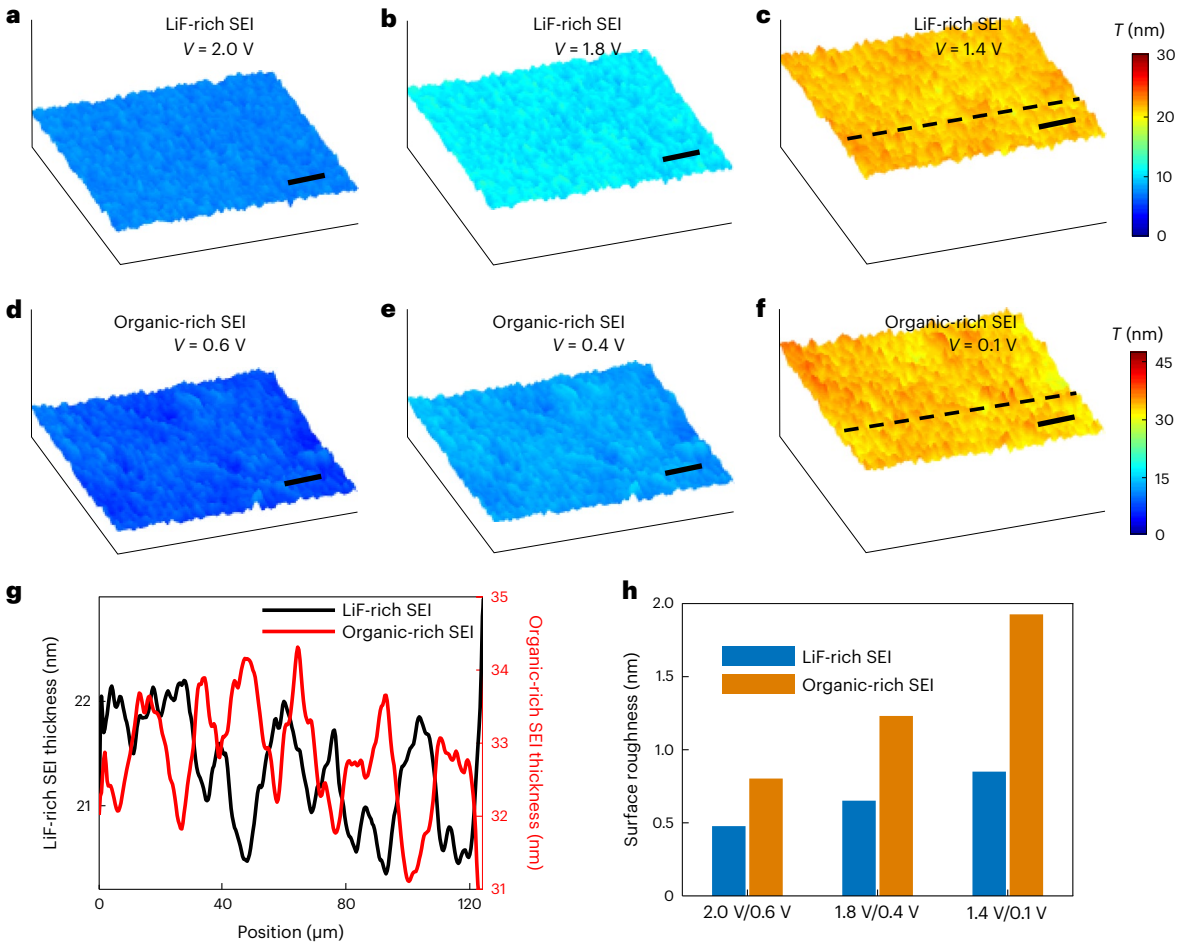

Fig. 4 | Imaging localized SEI formation dynamics using RIM. a–c, Morphology maps of the LiF-rich layer in 1 M $LiPF_6$/PC with 50 ppm H_2O at potentials $V = 2.0$ V (**a**), $V = 1.8$ V (**b**) and $V = 1.4$ V (**c**). **d–f**, Morphology maps of the organic-rich SEI layer in 1 M $LiPF_6$/PC with 50 ppm H_2O at potentials $V = 0.6$ V (**d**), $V = 0.4$ V (**e**) and $V = 0.1$ V (**f**). *T*, thickness. **g**, Thickness profiles of the LiF-rich layer (left axis and black line) and organic-rich layer (right axis and red line) along the same line, shown in **c** and **f** as a dashed black line. **h**, The surface roughness of the LiF-rich and organic-rich layers shown in **a–f**. Scale bars, 20 μm.

and apparently benefit from the generation of HF (equation (2)). The LiF-rich SEI layer continues to develop on the electrode surface after the first cycle but at a slower rate (~3.5 nm per cycle; Fig. 2b), since the thick layer of LiF generated in the first cycle reduces further charge transfer across the interface. The LiF-rich proto-SEI layer will contain tiny crystal domains[52–54], and the grain boundaries between these domains may facility charge transfer[55,56].

By comparison, the electrolyte without additional water behaves quite differently. In the first cycle, a thinner LiF-rich layer (~10 nm) is deposited onto the Cu electrode surface, demonstrating the relationship between the water content and the origin of greater LiF deposition. Trace water (~20 ppm) is always present in liquid electrolytes, even after the solvents have been rigorously dried[40]. After the first cycle in the electrolyte without the water additive, the deposition rate of the LiF layer remained greater (~5.0 nm per cycle; Fig. 2c) than that with the 50 ppm water additive (~3.5 nm per cycle; Fig. 2b). This indicates that the quality of such a LiF-rich SEI layer generated in the absence of water is less effective in insulating electrons, necessitating additional LiF deposition on the electrode in each of the subsequent cycles. Meanwhile, all three cycles share a similar EDL formation signal (Fig. 1c, section II, highlighted with blue shading), indicating that the difference in SEI quality has no effect on the charge arrangement on the electrode–SEI layer, which is essentially capacitive in nature and is unaffected by the SEI chemistry.

Another essential feature of the SEI is its organic-rich layer, which controls the total electrolyte consumption in irreversible and parasitic processes. We calculated the thickness of the organic-rich layer formed in each cycle and show it in Fig. 2b,c (orange colour bars). The organic-rich layer will be substantially eliminated during the re-oxidation process when the potential is scanned in the positive direction in each cycle. The organic-rich SEI layer formed in the first cycle is approximately 35 nm in the presence of 50 ppm water. As more LiF is deposited onto the electrode surface, the thickness of the organic-rich deposition layer in each cycle quickly decreases (Fig. 2b). In the absence of 50 ppm water, however, this thickness is generally consistent throughout the cycles (Fig. 2c). This finding connects water content to SEI quality and irreversible electrolyte consumption.

Chemical composition analysis of the SEI layer

To understand the chemical compositions and structure of the SEI layer, we performed XPS analysis on different SEI samples, including samples prepared at 1.4 V (after the formation of the LiF-rich proto-SEI) and at 0.1 V (after the formation of the organic-rich outer SEI; more details of the sample preparation are in Supplementary Section 7). Following the SEI's formation, the samples were thoroughly cleaned with DMC before being moved directly from the glove box to the XPS equipment without exposure to ambient air to avoid oxidation and contamination.

First, we study the effect of water additives on the SEI layer. The SEIs were generated by negatively scanning the electrode from 2.3 V to 0.1 V in electrolytes with (50 ppm) and without the water additive. The result shows an obvious change in composition. Fluorine (F) is the

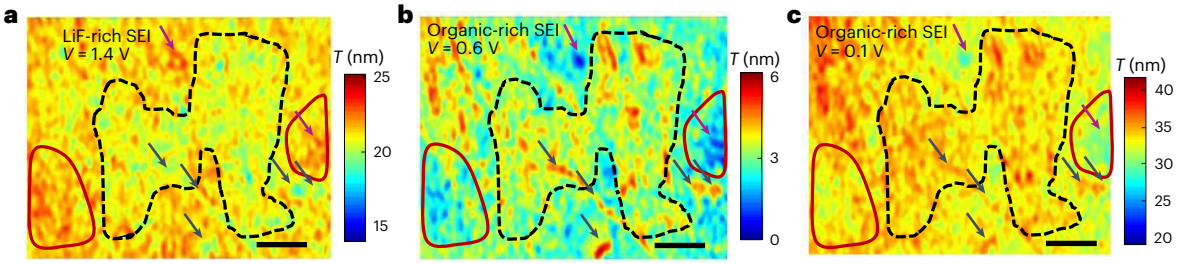

Fig. 5 | The spatial correlation between the LiF-rich and the organic-rich SEI layers. a, The LiF-rich layer's morphology at $V = 1.4$ V. Black dashed circle, thin LiF-rich layer region; red solid circle, thick LiF-rich layer regions; black arrows, thin LiF-rich layer locations; purple arrows, thick LiF-rich layer locations. **b**,**c**, Organic-rich SEI morphology at an early stage of deposition ($V = 0.6$ V, **b**) and late stage of deposition ($V = 0.1$ V, **c**). Black dashed circle, red solid circles, black arrows and purple arrows indicate the same regions or locations as in **a**. Scale bars, 20 µm.

dominating element (36%) in the SEI layer prepared with water additive (yellow bars in Fig. 3b). The SEI layer generated in the electrolyte without the water additive, on the other hand, has a very low concentration of F and a very high concentration of C and O elements (orange bars in Fig. 3b), with concentrations of 10%, 34% and 33%, respectively. The results directly confirm that water additives may effectively modify SEI compositions and promote the formation of a LiF-rich proto-SEI.

Second, the chemical compositions of the LiF-rich proto-SEI layer and the organic SEI layer are compared. Figure 3a,b summarizes the compositional and structural differences between SEI sample no. 1, formed by scanning from 2.3 V to 1.4 V, in which the LiF-rich proto-SEI dominates the SEI layer, and SEI sample no. 2, formed by scanning from 2.3 V to 0.1 V, in which the organic SEI layer is deposited on the electrode surface as well. The XPS wide scan spectra presented in Fig. 3a demonstrate a clear difference between these two SEI samples. Further elemental analysis shown in Fig. 3b shows that in SEI sample no. 1 (the potential stopped at 1.4 V; blue bars in Fig. 3b), the F element accounted for about 48% of the SEI produced, showing that LiF is the major component (blue bars for Li and F in Fig. 3b). However, in SEI sample no. 2 (the potential held at 0.1 V; yellow bars in Fig. 3b), the F percentage declines but the C and O contents rise to 18% and 20%, respectively. This is caused by the formation of organic species (ROCOOLi, RCOOLi and so on) in the SEI layer. These findings support our hypothesis that the inner proto-SEI layer is dominated by LiF, and that when the electrode is negatively polarized to 0.1 V, the solvent is reduced and organic species are generated.

Third, we have further confirmed the structure of the SEI by performing compositional depth profiling of the SEI layer by XPS sputter etching (Supplementary Section 7 for experimental details). Potential changes occur in the interfacial chemistry when using monoatomic Ar^+ ions for sputtering delicate SEI layers. Therefore, to minimize this effect, we chose to use monoatomic Ar^+ ions at very low incident energies of 300 eV and rastered the ion beam over a large area of the samples to minimize undesired chemical modifications. The sample was prepared in an electrolyte including a water additive, and the potential was scanned from 2.3 V to 0.1 V. Both LiF-rich and organic-rich layers were generated in this sample. Figure 3c,d shows the species detected at different depths of the SEI layer (for example, LiF, Li_2CO_3, Li_2O, ROCOOLi and so on). A relatively substantial quantity of organic species, such as ROCOOLi and RCOOLi, are identified on the surface of the SEI layer (no sputtering; Fig. 3c), along with certain inorganic species, such as LiF, Li_2O and Li_2CO_3. Almost no organic species can be discovered after removing the top layer of the SEI with a 450 s sputtering duration (estimated removing thickness of 8 nm; see more discussions in Supplementary Section 7). Instead, inorganic species such as LiF, Li_2CO_3 and Li_2O become dominant. This finding indicates that when the potential is scanned to 0.1 V, the organic component forms on top of the LiF-rich proto-SEI layer (Supplementary Figs. 15 and 16).

Spatial correlations between the LiF-rich and organic SEI

The optical reflectance curves in Figs. 1 and 2 are averaged across the entire observation window (80 µm by 120 µm), but the local heterogeneity has been smoothed off. The morphologies of the LiF-rich and organic-rich layers in the SEI at three different potentials were mapped using RIM, as illustrated in Fig. 4a–f and Supplementary Videos 1 and 2. LiF begins to develop on the Cu electrode at 2.0 V, with an average thickness of 5 nm and a surface roughness of 0.5 nm (standard deviation; Fig. 4h). Following the initial deposition, the LiF-rich layer grows to 12 nm at 1.8 V (Fig. 4b) and 23 nm at 1.4 V (Fig. 4c). Surface roughness increases proportionally to 0.7 nm at 1.8 V and 0.9 nm at 1.4 V (Fig. 4h). The organic-rich layer begins to develop at 0.6 V (Fig. 4d). The average thickness and surface roughness grow rapidly as the potential decreases (Fig. 4d–f,h), and the thickness of the organic layer in the SEI can approach 35 nm.

The deposition of a LiF-rich layer will have a major impact on surface reactions, including the growth of an organic-rich layer. To further understand the relationship between these two layers, we plotted the height profiles of the LiF-rich layer and the organic-rich layer in Fig. 4g along the same line (along the black dashed lines in Fig. 4c,f). There is a strong inverse spatial correlation when the LiF-rich layer is thin and the organic layer is rather thick, and vice versa. While the thickness variation in the LiF-rich layer is relatively small (~5%), the thickness variation in the corresponding organic SEI layer is likewise small (~6%). In addition, the SEI layer is not a perfect layer, since it contains many tiny crystal domains[52,54]. As a result, the tunnelling current does not dominate the electron source. Instead, the predominant contribution of leakage current is across grain boundaries. To further illustrate such relationships, we showed the thickness maps of these two layers individually in Fig. 5. The region circled by the black dashed line exhibits a thinner LiF-rich inorganic layer (Fig. 5a) and a thicker organic-rich SEI layer (Fig. 5b,c). The regions circled by the red solid line have a thicker LiF-rich inorganic layer (Fig. 5a) and a thinner organic-rich SEI layer (Fig. 5b,c). The inverse relation is more pronounced when we compare smaller electrode areas. The purple and black arrows represent regions with thicker and thinner LiF-rich inorganic SEI layers, respectively (Fig. 5a), while the corresponding regions in organic-rich layer maps (Fig. 5b,c) exhibit opposite responses.

It is commonly accepted that the inorganic layer (mostly LiF rich) in SEI is the primary component that prevents electron transport while allowing Li ions to diffuse through it. However, depending on the quality and thickness of the LiF-rich layer, a limited number of electrons can still tunnel through the LiF layer and induce the parasitic reactions, causing the gradual growth of the organic-rich outer layer. A thicker LiF layer will more efficiently block electrons and result in a thinner organic-rich outer layer, whereas a thinner LiF layer will result in less efficient electron blocking and a thicker organic-rich layer. In addition,

https://doi.org/10.1038/s41565-023-01316-3

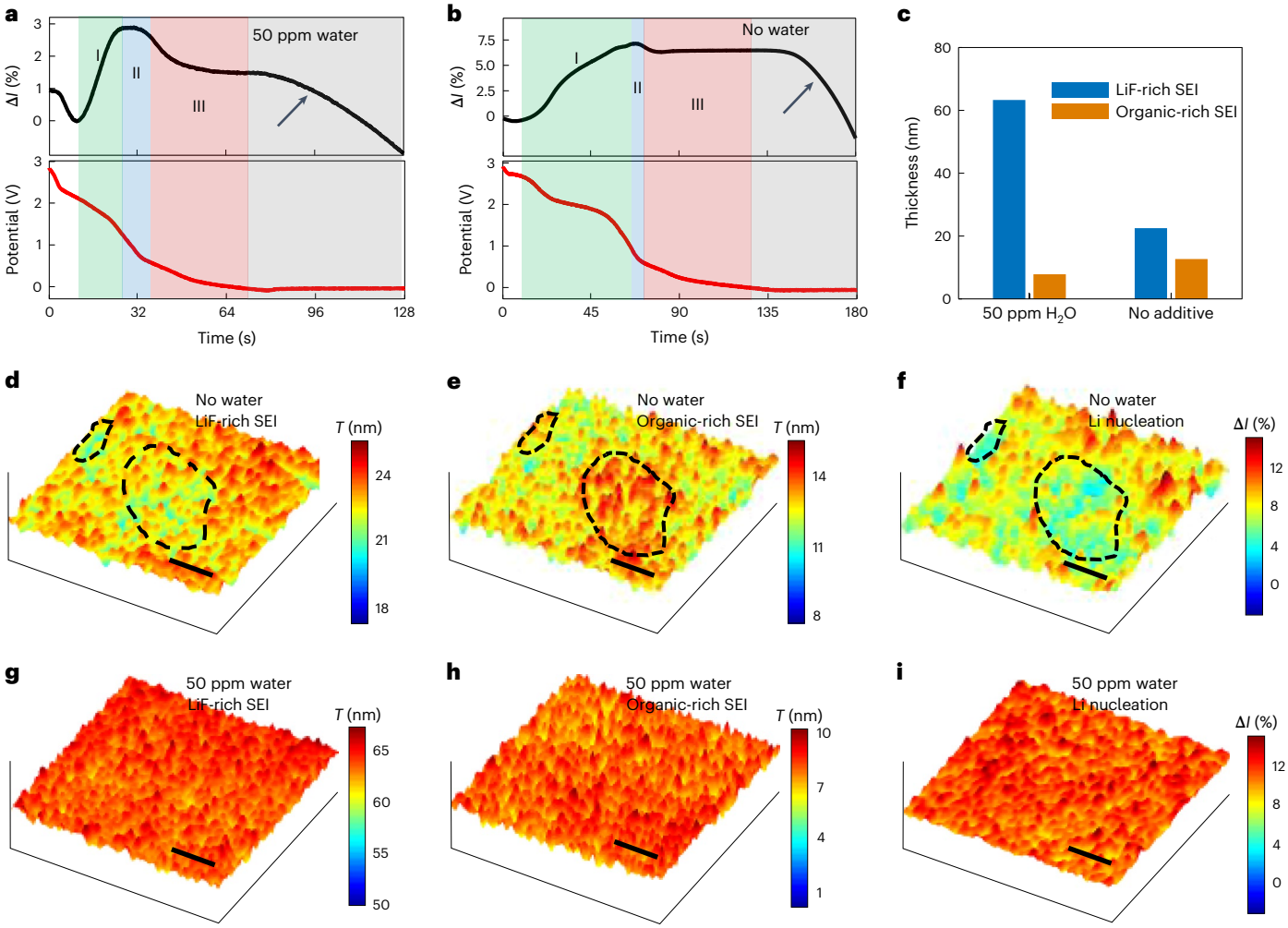

Fig. 6 | SEI affects the Li nucleation process. a,**b**, The RIM and the corresponding potentials in galvanostatic electrodeposition in 1 M $LiPF_6$/PC with 50 ppm H_2O (**a**) and without water additive (**b**). The experiment was performed with constant current at 0.1 mA cm^{-2} (voltages at the end of deposition are -40 mV and −42 mV, respectively). The top panels are the optical reflection responses during the measurement, and the bottom panels are the corresponding potentials. Sections I, II and III correspond to the formation processes of the LiF-rich SEI layer, EDL and organic-rich SEI layer. Please see more discussions in the main text. **c**, The thicknesses of the LiF-rich and organic-rich layers are extracted from the experiments shown in **a** and **b**. **d**–**f**, Morphology maps of the LiF-rich SEI layer (**d**) and the organic-rich SEI layer (**e**), and the optical response of Li nucleation (**f**) in the electrolyte without the water additive. **g**–**i**, Morphology maps of the LiF-rich SEI layer (**g**) and the organic-rich SEI layer (**h**), and the optical response of Li nucleation (**i**) in the electrolyte with the 50 ppm water additive. Note that Δ*I* in **f** and **i** is the intensity change caused by the Li nucleation, and the bigger Δ*I* means more Li nucleation. Scale bars, 20 μm.

we observe that the SEI layer thickness varies at the micrometre scale (Figs. 4 and 5). We believe the intrinsic stochasticity can lead to this non-uniform SEI deposition and geometrical evolutions even when the macroscopic conditions are very similar, and the Cu electrode was carefully cleaned (Supplementary Section 1). Previous research reported by Zhang et al.[57] also shows that morphology variations and localized electric field differences at the micrometre scale can still be observed on clean Cu foils. The potential stochasticity includes the variation of local electric field strength, thermal fluctuation of molecular transport, the discrete nature of reactions and statistics of the nucleation and deposition sites. In particular, the thickness fluctuation we observed is relatively small, only ~5% of the total thickness of the SEI layer (1.1 nm/22 nm from Fig. 4g).

We also extract the growth rates of the SEI layers using the RIM data. Supplementary Fig. 17 shows the growth rates of the LiF-rich SEI layer (red curve in Supplementary Fig. 17) and organic-rich SEI layer (blue curve in Supplementary Fig. 17) at different potentials. The growth rate of the LiF-rich layer quickly increases to the maximum value (~3 nm s^{-1}) and then slowly decreases to 0. However, the growth rate of the organic-rich SEI layer is not zero at 0.1 V. The results show that the reduction of the electrolyte is still ongoing even though the potential is very close to the Li nucleation potential. This indicates that during the initial Li nucleation, the organic-rich SEI deposition could still be in progress, and the SEI layer is dynamically changing while the Li nucleation is initiating.

SEI effects on Li nucleation

The heterogeneity of the SEI in chemical composition and morphology has a direct impact on Li nucleation and growth[58], which are closely connected to the performance of all Li-based battery chemistries. We generated Li deposition by polarizing the Cu electrode further down to lower potentials while using RIM to correlate the SEI quality and the subsequent Li nucleation dynamics in the absence or presence of the water additive. Galvanostatic electrodeposition was applied to generate the SEI and induce Li nucleation. The optical signal (top) and corresponding voltage signal (bottom) during these processes are shown in Fig. 6a,b in the presence and absence of an additional 50 ppm water additive, respectively. Sections I–III of the figure panels can each

be identified, which matches well with our prior CV experiments and confirms that the SEI layers formed in either a galvanostatic or potentiodynamic (CV) manner exhibit similar optical responses under RIM, showing RIM's universal reliability. The thicknesses of the LiF-rich and organic-rich layers, which are much thicker than the layers formed in the CV scans, were also extracted (Fig. 6c). This is because there is enough time at each potential in constant current mode for sufficient reactions to occur on the electrode surface (see more discussions in Supplementary Section 8).

When the potential of the working electrode falls below 0 V, the optical signals begin to decline (as indicated by the black arrows in Fig. 6a,b) due to the formation of light-scattering Li nuclei. Figure 6f,i shows the optical intensity map of Li nucleation. Figure 6f corresponds to the snapshot image at 128 s, whereas Fig. 6i corresponds to the nucleation image at 180 s. In Fig. 6f,i, for better visualization, we flip the optical response such that the brighter intensity represents greater Li nucleation. Without the water additive, the Li nucleation is clearly not homogeneous in the electrolyte (Fig. 6f). The addition of 50 ppm water considerably improves homogeneity (Fig. 6i). Comparing the thickness maps of the LiF-rich layer (Fig. 6d,g) and the organic layer (Fig. 6e,h) shows that the electrolyte with the 50 ppm water additive causes both the LiF layer and the organic layer to be much more uniform, allowing for a more even distribution of Li nuclei.

Conclusion

This work introduces a dynamic, non-invasive, and operando imaging platform (RIM) for mapping the minimal and localized SEI information. The optical interference intensifies the signal, allowing us to probe the localized responses from the stratified SEI structure and their evolution throughout cell cycling. RIM also has the unique feature of quantitatively separating the signals generated by the LiF-rich and organic-rich SEI subcomponents, resulting in a reliable descriptor for evaluating SEI quality. RIM is a unique platform that provides localized and dynamic interphasial information at any time point, which enables information to be found over the entire reaction process at the same location. This will allow us to study the interactions of different interphasial processes, including the LiF-rich and organic-rich SEI layers' formation, charge accumulation and Li nucleation. Equipped with this powerful technique, we discovered a strong inverse relationship between the LiF-rich inner layer and the organic-rich outer layer, with trace water (50 ppm) promoting the former and suppressing the latter. The inorganic layer is the most important subcomponent in homogenizing the Li nucleation distribution. This fundamental knowledge offers a strong foundation for designing better electrolytes and interphases for high-performance LMBs.

Online content

Any methods, additional references, Nature Portfolio reporting summaries, source data, extended data, supplementary information, acknowledgements, peer review information; details of author contributions and competing interests; and statements of data and code availability are available at https://doi.org/10.1038/s41565-023-01316-3.

References

1. Goodenough, J. B. & Park, K. S. The Li-ion rechargeable battery: a perspective. *J. Am. Chem. Soc.* **135**, 1167–1176 (2013).
2. Dunn, B., Kamath, H. & Tarascon, J. M. Electrical energy storage for the grid: a battery of choices. *Science* **334**, 928–935 (2011).
3. Grande, L. et al. The lithium/air battery: still an emerging system or a practical reality? *Adv. Mater.* **27**, 784–800 (2015).
4. Lu, Y. Y. et al. Stable cycling of lithium metal batteries using high transference number electrolytes. *Adv. Energy Mater.* **5**, 1402073 (2015).
5. Arico, A. S., Bruce, P., Scrosati, B., Tarascon, J. M. & Van Schalkwijk, W. Nanostructured materials for advanced energy conversion and storage devices. *Nat. Mater.* **4**, 366–377 (2005).
6. Sun, Y. M., Liu, N. A. & Cui, Y. Promises and challenges of nanomaterials for lithium-based rechargeable batteries. *Nat. Energy* **1**, 16071 (2016).
7. Cheng, X. B. & Zhang, Q. Dendrite-free lithium metal anodes: stable solid electrolyte interphases for high-efficiency batteries. *J. Mater. Chem. A* **3**, 7207–7209 (2015).
8. Tarascon, J. M. & Armand, M. Issues and challenges facing rechargeable lithium batteries. *Nature* **414**, 359–367 (2001).
9. Guo, Y. P., Li, H. Q. & Zhai, T. Y. Reviving lithium-metal anodes for next-generation high-energy batteries. *Adv. Mater.* **29**, 1700007 (2017).
10. Yuan, S. Y. et al. Graphene-supported nitrogen and boron rich carbon layer for improved performance of lithium-sulfur batteries due to enhanced chemisorption of lithium polysulfides. *Adv. Energy Mater.* **6**, 1501733 (2016).
11. Janek, J. & Zeier, W. G. A solid future for battery development. *Nat. Energy* **1**, 16141 (2016).
12. Luntz, A. C., Voss, J. & Reuter, K. Interfacial challenges in solid-state Li ion batteries. *J. Phys. Chem. Lett.* **6**, 4599–4604 (2015).
13. Cao, R. G., Xu, W., Lv, D. P., Xiao, J. & Zhang, J. G. Anodes for rechargeable lithium-sulfur batteries. *Adv. Energy Mater.* **5**, 1402273 (2015).
14. He, P., Zhang, T., Jiang, J. & Zhou, H. S. Lithium-air batteries with hybrid electrolytes. *J. Phys. Chem. Lett.* **7**, 1267–1280 (2016).
15. Huang, C.-J. et al. Decoupling the origins of irreversible coulombic efficiency in anode-free lithium metal batteries. *Nat. Commun.* **12**, 1452. (2021).
16. Qiao, Y. et al. A high-energy-density and long-life initial-anode-free lithium battery enabled by a Li_2O sacrificial agent. *Nat. Energy* **6**, 653–662 (2021).
17. Xu, K. Nonaqueous liquid electrolytes for lithium-based rechargeable batteries. *Chem. Rev.* **104**, 4303–4417 (2004).
18. Peled, E. The electrochemical behavior of alkali and alkaline earth metals in nonaqueous battery systems—the solid electrolyte interphase model. *J. Electrochem. Soc.* **126**, 2047 (1979).
19. Gauthier, M. et al. Electrode–electrolyte interface in Li-ion batteries: current understanding and new insights. *J. Phys. Chem. Lett.* **6**, 4653–4672 (2015).
20. An, S. J. et al. The state of understanding of the lithium-ion-battery graphite solid electrolyte interphase (SEI) and its relationship to formation cycling. *Carbon* **105**, 52–76 (2016).
21. Orsini, F. et al. In situ scanning electron microscopy (SEM) observation of interfaces within plastic lithium batteries. *J. Power Sources* **76**, 19–29 (1998).
22. Mehdi, B. L. et al. Observation and quantification of nanoscale processes in lithium batteries by operando electrochemical (S) TEM. *Nano Lett.* **15**, 2168–2173 (2015).
23. Nie, M. Y. et al. Lithium ion battery graphite solid electrolyte interphase revealed by microscopy and spectroscopy. *J. Phys. Chem. C* **117**, 1257–1267 (2013).
24. Wang, L. et al. Identifying the components of the solid–electrolyte interphase in Li-ion batteries. *Nat. Chem.* **11**, 789–796 (2019).
25. Ai, Q. et al. Lithium-conducting covalent-organic-frameworks as artificial solid-electrolyte-interphase on silicon anode for high performance lithium ion batteries. *Nano Energy* **72**, 104657 (2020).
26. Zeng, X. et al. Electrolyte design for in situ construction of highly Zn^{2+}-conductive solid electrolyte interphase to enable high-performance aqueous Zn-ion batteries under practical conditions. *Adv. Mater.* **33**, 2007416 (2021).
27. Nanda, J. et al. Unraveling the nanoscale heterogeneity of solid electrolyte interphase using tip-enhanced Raman spectroscopy. *Joule* **3**, 2001–2019 (2019).

28. Chen, D. et al. Origin of extra capacity in the solid electrolyte interphase near high-capacity iron carbide anodes for Li ion batteries. *Energy Environ. Sci.* **13**, 2924–2937 (2020).
29. Qiu, H. et al. Zinc anode-compatible in-situ solid electrolyte interphase via cation solvation modulation. *Nat. Commun.* **10**, 5374 (2019).
30. Wood, K. N. et al. Operando X-ray photoelectron spectroscopy of solid electrolyte interphase formation and evolution in Li_2S-P_2S_5 solid-state electrolytes. *Nat. Commun.* **9**, 2490 (2018).
31. Cheng, D. et al. Unveiling the stable nature of the solid electrolyte interphase between lithium metal and LiPON via cryogenic electron microscopy. *Joule* **4**, 2484–2500 (2020).
32. Cao, C. et al. Solid electrolyte interphase on native oxide-terminated silicon anodes for Li-ion batteries. *Joule* **3**, 762–781 (2019).
33. Zhou, Y. et al. Real-time mass spectrometric characterization of the solid–electrolyte interphase of a lithium-ion battery. *Nat. Nanotechnol.* **15**, 224–230 (2020).
34. Li, Y. Z. et al. Atomic structure of sensitive battery materials and interfaces revealed by cryo-electron microscopy. *Science* **358**, 506–510 (2017).
35. Wang, X. F. et al. New insights on the structure of electrochemically deposited lithium metal and its solid electrolyte interphases via cryogenic TEM. *Nano Lett.* **17**, 7606–7612 (2017).
36. Wan, J. et al. Ultra-thin solid electrolyte interphase evolution and wrinkling processes in molybdenum disulfide-based lithium-ion batteries. *Nat. Commun.* **10**, 3265 (2019).
37. von Cresce, A., Russell, S. M., Baker, D. R., Gaskell, K. J. & Xu, K. In situ and quantitative characterization of solid electrolyte interphases. *Nano Lett.* **14**, 1405–1412 (2014).
38. Pathak, R. et al. Fluorinated hybrid solid-electrolyte-interphase for dendrite-free lithium deposition. *Nat. Commun.* **11**, 93 (2020).
39. Liu, T. et al. In situ quantification of interphasial chemistry in Li-ion battery. *Nat. Nanotechnol.* **14**, 50–56 (2019).
40. Nie, M. et al. Role of solution structure in solid electrolyte interphase formation on graphite with $LiPF_6$ in propylene carbonate. *J. Phys. Chem. C* **117**, 25381–25389 (2013).
41. Qian, J. et al. Dendrite-free Li deposition using trace-amounts of water as an electrolyte additive. *Nano Energy* **15**, 135–144 (2015).
42. Shen, C. et al. Li_2O-reinforced solid electrolyte interphase on three-dimensional sponges for dendrite-free lithium deposition. *Front. Chem.* **6**, 517 (2018).
43. Terborg, L. et al. Ion chromatographic determination of hydrolysis products of hexafluorophosphate salts in aqueous solution. *Anal. Chim. Acta* **714**, 121–126 (2012).
44. Shi, Y. et al. Electrochemical impedance imaging on conductive surfaces. *Anal. Chem.* **93**, 12320–12328 (2021).
45. Foley, K. J., Shan, X. & Tao, N. J. Surface impedance imaging technique. *Anal. Chem.* **80**, 5146–5151 (2008).
46. Aurbach, D., Daroux, M., Faguy, P. & Yeager, E. Identification of surface films formed on lithium in propylene carbonate solutions. *J. Electrochem. Soc.* **134**, 1611 (1987).
47. Xing, L. et al. Theoretical investigations on oxidative stability of solvents and oxidative decomposition mechanism of ethylene carbonate for lithium ion battery use. *J. Phys. Chem. B* **113**, 16596–16602 (2009).
48. Kanamura, K. et al. Oxidation of propylene carbonate containing $LiBF_4$ or $LiPF_6$ on $LiCoO_2$ thin film electrode for lithium batteries. *Electrochim. Acta* **47**, 433–439 (2001).
49. von Cresce, A. et al. In situ and quantitative characterization of solid electrolyte interphases. *Nano Lett.* **14**, 1405–1412 (2014).
50. Aurbach, D. et al. The study of electrolyte solutions based on ethylene and diethyl carbonates for rechargeable Li batteries: I. Li metal anodes. *J. Electrochem. Soc.* **142**, 2873 (1995).
51. Parimalam, B. S., MacIntosh, A. D., Kadam, R. & Lucht, B. L. Decomposition reactions of anode solid electrolyte interphase (SEI) components with $LiPF_6$. *J. Phys. Chem. C* **121**, 22733–22738 (2017).
52. Li, Y. et al. Atomic structure of sensitive battery materials and interfaces revealed by cryo–electron microscopy. *Science* **358**, 506–510 (2017).
53. Huang, W., Wang, H., Boyle, D. T., Li, Y. & Cui, Y. Resolving nanoscopic and mesoscopic heterogeneity of fluorinated species in battery solid-electrolyte interphases by cryogenic electron microscopy. *ACS Energy Lett.* **5**, 1128–1135 (2020).
54. Wang, X. et al. New insights on the structure of electrochemically deposited lithium metal and its solid electrolyte interphases via cryogenic TEM. *Nano Lett.* **17**, 7606–7612 (2017).
55. Wang, A., Kadam, S., Li, H., Shi, S. & Qi, Y. Review on modeling of the anode solid electrolyte interphase (SEI) for lithium-ion batteries. *npj Comput. Mater.* **4**, 15 (2018).
56. Leung, K. & Jungjohann, K. J. Spatial heterogeneities and onset of passivation breakdown at lithium anode interfaces. *J. Phys. Chem. C* **121**, 20188–20196 (2017).
57. Zhang, Y. et al. Dendrite-free lithium deposition with self-aligned nanorod structure. *Nano Lett.* **14**, 6889–6896 (2014).
58. Kasse, R. M. et al. Understanding additive controlled lithium morphology in lithium metal batteries. *J. Mater. Chem. A* **8**, 16960–16972 (2020).

Methods

Operando RIM

The operando RIM instrument was built on an upright Olympus BX50 microscope in an argon-filled glove box (MBraun, with an H_2O and O_2 level of less than 0.5 ppm). The electrolytes have a relatively high refractive index (around 1.415 in our case) compared with that of air (~1), and this refractive index mismatch will lead to aberrations that blur the images. To minimize the influence of the refractive index mismatch, a special ×20 multi-immersion objective (Applied Scientific Instrumentation) was used. The objective can provide a refractive index match in a wide range from 1.33 to 1.56, which completely meets the imaging requirements in the electrolytes that are commonly used in LMBs and LIBs at present. The objective is immersed in the electrolyte in an open-cell set-up. The numerical aperture of the objective is around 0.68 in the electrolyte that has a refractive index of 1.415. The incident light is centred around 600 nm using a band pass filter (Supplementary Fig. 5). The spatial resolution of the RIM instrument is defined by the diffraction limit, and the temporal resolution is defined by our camera frame rate. Each pixel in the RIM maps is an average result from an area of 300 nm by 300 nm. To catch the electrochemical reaction process, we chose the frame rate of ~10 frames per second in this research, but the camera frame rate can be ramped up to 1,000 frames per second if necessary. During the experiment, the dynamic change in the SEI will induce interference and affect the reflected light intensity, which is recorded with a charge-coupled device (CCD) camera (Pike, F032C monochrome). The recorded images were synchronized with the electrochemical potentials and currents using a LabVIEW card (Supplementary Section 1). The camera was connected to a computer outside the glove box with a feedthrough cable, and the camera and the potentiostat were synchronized and controlled by the same computer. The light reflected from different surfaces of stratified SEI structure (Fig. 1a) will interfere with each other, which leads to localized optical intensity changes. Therefore, the opticla signal is closely related to the refractive index of the dielectric medium across the electrode/electrolyte interphase. When the SEI layers form on the electrode substrate, the reflected optical intensity will increase or decrease according to the refractive index change and is very sensitive to the thickness of the formed SEI layer.

Differential optical response

When the electrochemical reactions happen, the SEI layer will form on the electrode surface, and the optical reflectance measures the overall changes in the reaction. On the other hand, the integration of the electrochemical current quantifies all the electrochemical reactions that happen on the surface via coulomb counts. Therefore, a mathematical relation should exist between the current and the derivative of the optical signal, which signifies the electrochemical reactions that happen. Such a relation is revealed in Fig. 1e, where the derivative of the optical response (dI/dt) displays a 'fingerprint' match with the electrochemical current (black curve in Fig. 1d). This serves as strong quantitative evidence for the argument that what is optically detected does reflect the electrochemical reactions that happen on the electrode surface.

Relationship between optical reflectance and refractive index

When the light is reflected from different surfaces of a thin film, interference will happen and a phase difference will be introduced to influence the detected optical reflectance intensity. Depending on the refractive index difference between the surrounding environment and the newly formed layer, different degrees of constructive or destructive interference will occur. Thus, by detecting the reflected intensity change, we can easily recognize the characteristics of the SEI layer that is deposited on the substrate. In our system, the refractive index of the bulk electrolyte is 1.415. When the LiF-rich SEI (refractive index is 1.32) accumulates on the substrate, we will observe an increasing optical signal. When the organic-rich SEI (refractive index is around 1.46) forms, there will be a decreasing optical signal. Details are provided in Supplementary Section 2.

Converting reflectance to thickness

In order to convert the optical reflectance to the SEI layer thickness, we have established conversion curves (see detailed discussions in Supplementary Section 6). Based on the Fresnel equations, the Winspall software package is used to calculate the reflectivity from multilayer interference. A dual-layer model of the SEI structure is adopted, and the parameters for simulation are summarized in Supplementary Table 1. The calculation results in Supplementary Fig. 13 elucidate how to convert the RIM signal to the SEI layer thickness. To verify the RIM, we have performed control experiments using poly(methyl methacrylate) (PMMA) thin film (Supplementary Section 2). The thickness of the PMMA thin film was measured using both RIM and the profilometer, and the results show excellent agreement between the two methods (Supplementary Figs. 3 and 4). In addition, we have also calibrated the optical properties of the SEI layer using both RIM and AFM images (see more discussions in Supplementary Fig. 7).

Morphology analysis

The morphology and thickness of the SEI layers are obtained through the conversion curves established from the experiments shown in Supplementary Fig. 13. We have synchronized the optical images with the applied electrochemical potentials (see more discussions in Supplementary Section 1); each frame of the RIM images can be correlated to certain time point in SEI formation dynamic process. For example, the total amount of reflectance change caused by the LiF-rich SEI is calculated by subtracting the initial reflection image (first frame of the entire sequence) from the last frame at the end of section I. Then we convert the intensity value of each pixel to thickness using the calibration curves and plot the morphology maps (such as Figs. 4a–f, 5 and 6d,e,g,h). The morphology and localized information of the LiF-rich SEI are thereby achieved. Similarly, the difference between the last frame and the first frame in section III represents the reflectance changes caused by the organic-rich SEI formation on the electrode surface.

Data availability

All the data used to plot the figures are available via zenodo.org.

Acknowledgements

X.S. acknowledges the funding support from the start-up fund at the University of Houston, the University of Houston's Center for Carbon Management in Energy, UL Research Institutes, Beyond Bits Technology, the US Department of Agriculture's Small Business Innovation Research programme (awards no. 2022-70012-36900 and no. 2019-33610-29769) and University Training and Research for Fossil Energy Applications (US Department of Energy DE-FE-0032092). The work performed at Pacific Northwest National Laboratory (PNNL) was supported by the Assistant Secretary for Energy Efficiency and Renewable Energy, and Vehicle Technologies Office of the US Department of Energy through the Advanced Battery Materials Research programme under contract no. DE-AC05-76RL01830. PNNL is operated by Battelle for the US Department of Energy under contract no. DE-AC05-76RL01830. Y.Y. acknowledges the funding support from the US Department of Energy's Office of Energy Efficiency and Renewable Energy under the Vehicle Technologies Program under contract no. DE-EE0008864. K.X. acknowledges the support from the Joint Center for Energy Storage Research, an energy hub funded by the US Department of Energy's Basic Energy Sciences programme. X.S. thanks Z. Zhu from PNNL for his insightful discussions of SEI formation, and thanks P. Ruchhoeft for providing the thermal evaporator for the electrode fabrication.

Author contributions

X.S., W.X., Y.Y. and K.X. conceived the idea and designed the research. X.S. supervised the research. G.F. carried out and managed most of

the experiments, including performing all the RIM measurements on SEI formation and Li nucleation, characterizing the SEI chemical compositions using XPS and conducting atomic force microscopy and profilometer calibrations. G.F. analysed the data and prepared the figures. H.J. prepared the electrolytes, electrochemical depositions of SEI and Li on Cu foils and samples for XPS depth profiling. Y.S. helped with RIM instrument development and data analysis. M.H.E. performed the XPS depth profiling experiment and provided insight to understand the data. X.Y., Y.Z., Y.L. and C.Y. provided suggestions on the experiments. Y.L. provided insight on understanding the RIM response. X.S., G.F., W.X., Y.Y. and K.X. discussed the data and wrote the manuscript.

Competing interests

X.S. has equity interest in Pani Clean, Inc. Y.Y. has equity interest in LiBeyond, LLC and Solid Design Instruments, LLC. Y.L. has equity interest in LiBeyond, LLC. The University of Houston reviewed and approved their relationship in compliance with its conflict-of-interest policy. The remaining authors declare no competing interests.

Additional information

Supplementary information The online version contains supplementary material available at https://doi.org/10.1038/s41565-023-01316-3.

Correspondence and requests for materials should be addressed to Kang Xu, Yan Yao, Wu Xu or Xiaonan Shan.

Peer review information *Nature Nanotechnology* thanks the anonymous reviewers for their contribution to the peer review of this work.